Pakistan Academy of Sciences

Review Article

Analytical Techniques for Elemental Analysis: LIBS, LA-TOF-MS, EDX, PIXE, and XRF: A Review

Muhammad Aslam Baig[1]*, Amir Fayyaz[1], Rizwan Ahmed[2], Zeshan Adeel Umar[2], Haroon Asghar[2], Usman Liaqat[3], Rinda Hedwig[4], and Koo Hendrik Kurniawan[4]

[1]Atomic and Molecular Physics Laboratory, Quaid-i-Azam University, Islamabad, Pakistan

[2]National Centre for Physics, Quaid-i-Azam University Campus, 45320 Islamabad, Pakistan

[3]School of Chemical and Materials Engineering, National University of Sciences
and Technology (NUST), Islamabad, Pakistan

[4]Research Centre of Maju Makmur Mandiri Foundation, 40/80 Srengseng Raya,
Jakarta 11630, Indonesia

Abstract: This contribution presents the applications of laser-induced breakdown spectroscopy (LIBS) for qualitative and quantitative elemental analysis of several samples such as geological ores, cement, and industrial materials. A combination of LIBS with the laser ablation time–of–flight mass spectrometer (LA-TOF-MS) assists in elemental quantification and isotopic abundance analysis. Different elemental components such as aluminum (Al), calcium (Ca), iron (Fe), potassium (K), lithium (Li), magnesium (Mg), sodium (Na), rubidium (Rb), silicon (Si), strontium (Sr), and titanium (Ti) in cement varieties, as well as rare earth metals, lanthanum (La), cerium (Ce), and neodymium (Nd) in geological ore samples, and cobalt (Co), chromium (Cr), nickel (Ni), iron (Fe), and molybdenum (Mo) in industrial standard material samples, have been precisely identified and their relative weight percentages estimated using CF-LIBS and LA-TOF-MS diagnostic techniques. To ensure the reliability of LIBS for the elemental analysis of industrial materials, a comparative study with other compatible techniques, including EDX, PIXE, and XRF, utilizing different excitation sources is presented. The results suggest that LIBS offers unique advantages, enabling rapid elemental analysis in circumstances where other techniques may face certain limitations.

Keywords: Calibration Free-LIBS, LA-TOF-MS, PIXE, XRF, EDX.

1. INTRODUCTION

Laser-induced breakdown spectroscopy (LIBS) is an analytical atomic emission spectroscopy technique. It is rapid, reliable, efficient, micro-destructive, and compatible with the elemental analysis of industrial [1, 2], geological [2], and pharmaceutical samples [3]. LIBS is based on the laws of quantum mechanics describing the discrete nature of atomic levels and the generation of a micro-plasma on the surface of the target sample [3-10]. LIBS employs high-power short laser pulses to create a high-temperature plasma on the target surface. Essentially, the laser beam is focused on the target surface, causing

a small portion of the sample to be ablated. This ablated material then interacts with the latter part of the laser pulse, leading to the formation of a highly energetic plasma comprising free electrons, ions, and neutral particles. As the plasma undergoes cooling, electrons in the excited states of atoms and ions make transitions to their characteristic ground states. This process results in the emission of light characterized by distinct spectral lines, bands, and an overarching continuum. These unique lines, which describe the material, have two primary characteristics; spectral lines at specific wavelengths and relative intensities. These factors depend on both the composition of the emitting

atoms and their atmosphere. The emitted light from the plasma is collected through a CCD/ICCD detection system covering a particular wavelength range. The LIBS data are then drawn as an emission spectrum using commercially available software. Characteristic LIBS spectral emission lines are associated with each element in the Periodic Table. The elemental composition of the trace and major elements in the sample can be quickly determined using the LIBS spectrum [11-15].

For the last couple of years, various LIBS research articles on elemental quantification analysis have been published using different LIBS techniques, such as Calibration Free-LIBS (CF-LIBS) including the Boltzmann plot technique, electron number-density conservation method, and Calibration Curve-LIBS (CC-LIBS) with ANN, univariate analysis, multiple linear-regression, PCA, PLS, and SVM [9, 10, 16-21]. CF-LIBS was first proposed by Ciucci *et al*. [11] for the elemental study of metallic alloys and the estimation of the chemical composition of the atmosphere. They proposed a mathematical model explaining the physical conditions of the laser-produced plasmas to estimate chemical composition. With CF-LIBS, referenced samples or calibration curves are unnecessary, and effective avoidance of matrix effects is possible. The application of the CF-LIBS technique involves taking into account the following key assumptions: ensuring identical chemical composition between plasmas and samples (i.e., stoichiometric ablation), expecting particles within the plasma, when elevated in energy levels, to adhere to the Boltzmann distribution (i.e., locally in thermal equilibrium), ensuring that spectral lines are devoid of self-absorption (optically thin plasma), and recording spectra that include all elemental species. The CF-LIBS method has been applied to examine various samples, including alloys containing Al, C-Fe, Fe, and Cu, as well as diverse geological and raw materials such as sedimentary rocks, pigments found on Roman frescoes and parchments, meteorites, glass, soil, kidney stones, cement, coral skeletons, and human hair. Nevertheless, the precision and accuracy of the CF-LIBS technique still need improvement [12-15, 22, 23].

In this review, analyses of various samples including geological ores containing rare earth metals, cement, and industrial alloys are presented.

The investigation involves qualitative studies through LIBS and quantitative analysis utilizing a combination of CF-LIBS, laser ablation time–of–flight mass spectrometry (LA-TOF-MS), energy dispersive X-ray (EDX), X-ray fluorescence (XRF), and proton-induced X-ray emission (PIXE) diagnostic analytical methods. The results obtained using CF-LIBS and LA-TOF-MS are compared and cross-validated with those obtained from EDX, XRF, and PIXE, focusing on major, minor, and trace constituent elements within different samples. The primary aim of this review is to explore the capabilities of LIBS for the chemical quantification of novel materials.

2.   MATERIALS AND METHODS

2.1. Calibration Free LIBS (CF-LIBS) Method

In the Calibration-Free LIBS (CF-LIBS) approach, the initial step for elemental analysis involves constructing Boltzmann plots using various spectroscopic parameters, such as the relative intensity of observed spectral lines, transition probability, upper-level energy, statistical weight, and central wavelength corresponding to the constituent elements. This process assumes that the plasma is in local-thermal equilibrium (LTE). The Boltzmann distribution function for the population density of the excited state can be expressed as follows [24-28]:

$$n_k^s = n^s \frac{g_k}{P(T)} \exp\left(-\frac{E_k}{k_B T}\right) \qquad (1)$$

Here, n_k^s represents the population concentration for the excited level k of the species s, n^s denotes the total concentration for elements s in an LTE plasma, g_k stands for the statistical mass for a transition of the upper-state, and $P(T)$ is the quantum statistical sum. The partition function, defined as $P(T) = \sum_k g_k \, exp(-E_k/k_B T)$, involves the summation of statistical weights up to the level k where the energy E_k is associated with the upper level, k_B signifies the Boltzmann constant, and T is the plasma temperature. In the context of an optically-thin plasma state, the intensity of an emission line I_{ki}^s is expressed as proportional to n_k^s. Incorporating this intensity relation in Equation (1), we get:

$$I_{ki} = A_{ki} n^s \frac{hc}{\lambda_{ki}} \frac{g_k}{P(T)} \exp\left(-\frac{E_k}{k_B T}\right) \qquad (2)$$

The measured intensity is directly influenced by the efficiency of the collecting method; hence, Equation (2) is formulated as:

$$\overline{I_{ki}} = FC^S A_{ki} \frac{g_k}{P(T)} \exp(-\frac{E_k}{k_B T}) \qquad (3)$$

Where, $\overline{I_{ki}}$ is the net integrated emission intensity of the spectral line, F is the experimental factor, i.e., depending on the efficiency of the collecting method and size of the LTE plasma, and C^S denotes the chemical weight of the emitted constituents. By ensuring a natural log on both sides of Equation (3) [20-27], the following relationship is obtained:

$$\ln[\frac{\lambda_{ki}\overline{I_{ki}}}{hcA_{ki}g_k}] = -\frac{E_k}{k_B T} + \ln[\frac{FC^S}{P(T)}] \qquad (4)$$

Equation (4) is a straight-line equation of the type, $y = bx + q_S$.

$$y = \ln[\frac{\lambda_{ki}\overline{I_{ki}}}{hcA_{ki}g_k}]; x = E_k; q_S = \ln[\frac{FC^S}{P(T)}] \qquad (5)$$

A Boltzmann plot can be characterized for each species by taking $\ln[\lambda_{ki}\overline{I_{ki}}/hcA_{ki}g_k]$ on the y-axis and E_k on the x-axis. In the Boltzmann plot, the reciprocal of the slope ($b = -1/k_B T$) yields the plasma temperature and q_S is determined from the intercept along the y-axis. Finally, the chemical weight of each element in the material is calculated from the resulting relationship:

$$C^S = \frac{1}{F}P(T)\exp(q_S) \qquad (6)$$

The Sah-Boltzmann equation can be applied to estimate the chemical weight of the ionic components present in the sample plasma. In brief, the following equation is used to calculate the chemical weight of each ionic constituent in the sample [28-32].

$$\frac{n^{\alpha,z}}{n^{\beta,z+1}} = \frac{I_{\alpha,z}}{I_{\beta,z+1}} \times \frac{P_{\alpha,z}}{P_{\beta,z+1}} \exp(-\frac{E_{k,\beta,z+1}+E_{k,\alpha,z}}{k_B T}) \qquad (7)$$

where, $E_{k,\alpha,z}$ and $E_{k,\alpha,z+1}$ represent the ionization energies of integral component α in charge states z and $z+1$, respectively. Similarly, $n^{\alpha,z}$, and $n^{\beta,z+1}$ denote the electron plasma number-density of element α in charge states z and $z+1$, respectively. In the same way, $P_{\alpha,z}$ and $P_{\beta,z+1}$ stand for the quantum statistical sum of the higher charge-state (z) and lower charge-state ($z+1$). The concentration contribution of any element in the sample is determined by summing up both neutral and ionic contributions. The individual contribution to the total chemical weight ratio of any element is then computed using the following relationship:

$$n^\alpha = n^{\alpha,z} + n^{\alpha,z+1} \qquad (8)$$

$$C^\alpha(\%) = \frac{n^\alpha}{\Sigma n^\alpha} \times 100 \qquad (9)$$

2.2. Materials

In this study, we investigated 5 geological samples containing rare earth elements, 7 samples of cement, and 4 molybdenum (Mo) based alloy samples for elemental analysis. The rare earth ore samples were collected from a mineralogical and geological site in the northern sectors of Gilgit-Baltistan, Pakistan. To prepare the samples for LIBS, we subjected them to a 40-minute ultrasonic bath with acetone, followed by drying in a furnace at 100 °C for 90 minutes to eliminate moisture. Subsequently, the target samples were excellently ground as a powder form to achieve reliable uniformity, and pellets having a surface area of ~0.95 cm² and a thickness of 0.5 cm were formed by applying a pressure of about 7 tons. Similarly, a total of seven cement samples labeled HS-1, HS-2, HS-3, HS-4, HS-5, HS-6, and HS-7 were obtained from various production facilities for cement in Pakistan. Pellets having a thickness of about 0.5 cm and a surface area of ~1.77 cm² were formed using a hydraulic press without the addition of any adhesive substance. For the Mo-based alloy samples with different compositions (purity > 99.95%), we employed arc melting in an environment enriched with argon gas within a copper hearth cooled by water. Before the insertion of pure argon, a vacuum of 10^{-6} mbar was established. A Ti–getter underwent melting for a duration of one minute to absorb any oxygen remnants prior to the real sample melting process. Each sample underwent five re-melting cycles, with flipping after each cycle to confirm chemical consistency. Although multiple samples were examined, this contribution focuses on presenting a detailed analysis of one representative sample from each category.

3. ANALYTICAL TECHNIQUES

3.1. Laser Induced Breakdown Spectroscopy (LIBS)
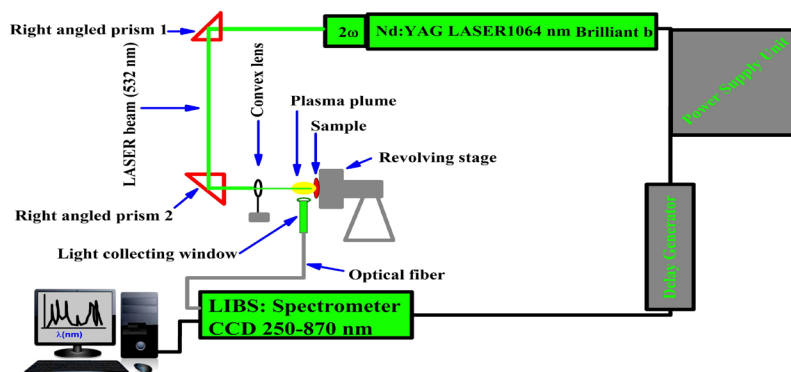
The custom-built tabletop LIBS experiments have

Fig. 1. A schematic diagram of the experimental setup of the LIBS system.

been performed by using a Q–switched Nd:YAG (Brilliant–B, Quantel (France)) laser beam (532 nm wavelength) having a pulse energy of 110 mJ, 10 Hz repetition frequency, and pulse interval of 5 ns that was concentrated by a converging lens of 10 cm focal length on the target surface to generate the plasma plume. Figure 1 shows an experimental arrangement for the LIBS analyses.

The sample was placed on a rotating stand, continuously revolving around an axis. The utilization of the rotating stand was preferred due to several advantageous effects. These included providing a clean area of the target substance to each single pulse, enhancing the replicability of mass ablation, averting the growth of intense trash, and avoiding non-uniformity of the target. The focused laser beam at the sample side had a spot size of around 0.5 mm, corresponding to a laser fluence of around 55 Jcm^{-2}. To capture the plasma optical spectrum, an optical fiber with a focusing lens (positioned vertically to the laser beam) featuring high–OH and a core diameter of approximately 600

µm was employed. Multiple compact spectrometers, each outfitted with a 10 µm slit-size in the detection system from Avantes, Holland, were utilized to capture the optical spectrum across the wavelength from 250 to 870 nm. A delay-time of 2 µs among the laser-beam emission and the reading of the detection setup was implemented, with a gate width of about 1 ms.

The time-resolved spectra of several elements were also recorded using a setup at the Maju Makmur Mandiri Research Center, Indonesia. In this setup, the light emission signal by the laser-produced plasma was captured using an optical fiber with a numerical aperture of 0.27 which was attached to a 1.0 m Czerny Turner type spectrograph outfitted with a 5.0 µm wide entrance slit and an 1800 grooves/mm grating. The resolution of this spectrograph at 313.1 nm is about 0.012 nm. The exit slit of the spectrograph was attached with a time-gated ICCD (intensified (Andor i–Star, UK) CCD, (1024) × (256) pixels,). To synchronize the delay time between the laser pulse and the ICCD, the
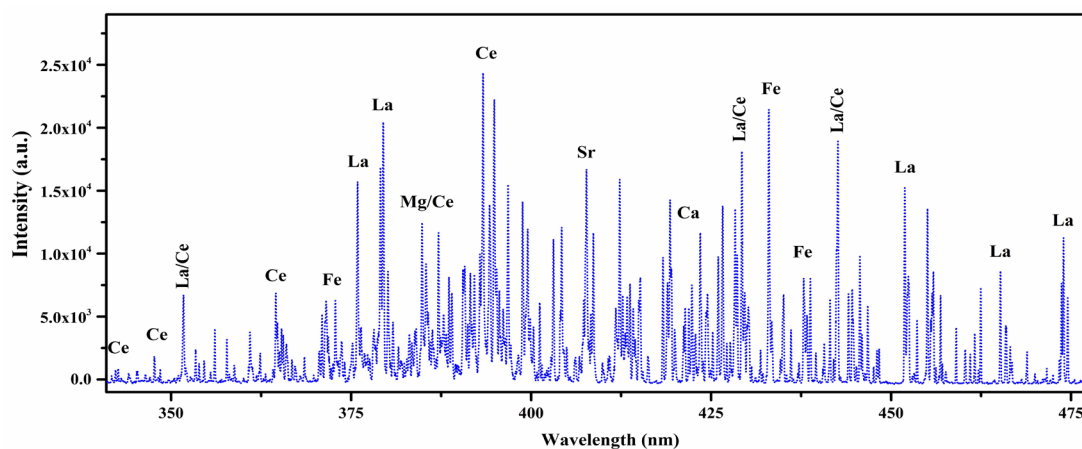

Fig. 2. LIBS emission spectrum of the rare earth geological sample from 335 nm to 480 nm wavelength region.

ICCD was triggered using an output signal from the laser system. The delay-time of the ICCD was set at 1 μs and the corresponding gate-delay was adjusted at 30 μs. Acquisition and analysis of the data were carried out with an individual computer system. All the experiments were conducted under atmospheric air pressure and the spectra were registered through the averaging of ten single-shot datasets under similar investigational circumstances, aiming to enhance the signal-to-noise ratio.

In Figure 2, we display the emission spectrum of the rare earth geological sample having a wavelength range from 335 nm to 480 nm. The emission spectrum shows the dominating emission lines of rare earths along with other elements such as Ca, Fe, Mg, Na, Si, and Ti. In Figure 3, the emission spectrum (covering the spectral range of 420-562 nm) of a cement sample is presented. The National Institute of Standards and Technology (NIST) database system [33] enabled the identification of each spectral line in the spectrum. In the cement test sample, the emission lines of Ca (I) and Ca (II) predominate, followed by Fe, K, Li, Mg, Na, Sr, and Ti. The signal height is indicative of the component concentration in the sample. A calibration-free LIBS procedure was employed for quantitative

analysis, depending on plasma parameters derived from Boltzmann plots of the essential elements. The calculated weight percentage (wt.%) of the Ca in the various cement samples is around (71-76 %). The wt.% of the other elements was estimated to be in the range of; Al (1-3%), Fe (3-8%), K (2-5%), Li (0.3-1.3%), Mg (1-3.9%), Na (1-4%), Si (6-14%), Sr (0.1-0.4%), and Ti (0.35-0.95%). Figure 4 displays the emission spectrum of the Mo-based alloy sample, containing the wavelength scale from 257 nm to 392 nm. The spectrum reveals the principal presence of Mo emission lines, with cobalt (Co), nickel (Ni), chromium (Cr), and iron (Fe) lines.

To perform quantitative analysis, the number-density of electron plasma (N_e) was determined by calculating the full width at half–maximum (FWHM) of the broadening of the Stark line using the well-recognized equation [12, 14, 21].

$$N_e = \frac{\Delta\lambda_{1/2}}{2\omega_s} \times 10^{16} \ (cm^{-3}) \tag{10}$$

Where the contribution of Stark broadening to the overall line profile is denoted by $\Delta\lambda^s_{FWHM} \ (nm)$ and the Stark broadening parameter by ω_s (nm).

Fig. 3. LIBS emission spectrum of the cement sample from wavelength section 420-562 nm at a laser wavelength of 532 nm, delay-time of 2 μs, and laser energy ~110 mJ.

Fig. 4. The LIBS spectrum of the alloy sample within the wavelength region from 257 nm to 392 nm.
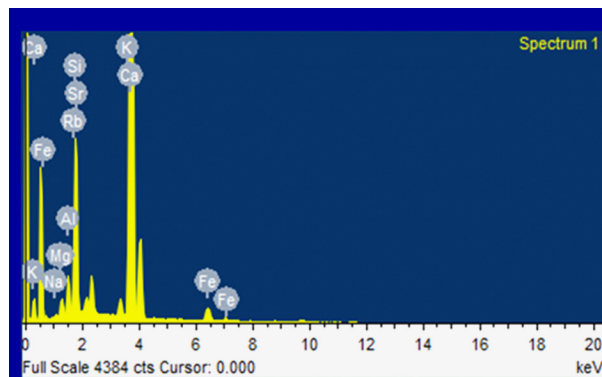
We have used the optically–thin emission line of neutral calcium (Ca I) at 610.27 nm to estimate the electron number density for all the cement samples. The broadening parameter of the specific Stark emission line (ω_s = 0.00698 nm) was sourced from existing literature [34]. A Voigt fitting considering the instrumental width factor (0.06 ± 0.01 nm) was used to determine the number-density of the electron plasma. The estimated N_e for the cement sample was about (1.1 ± 0.6) × 10^{17} cm⁻³. The McWhirter's criterion in which the collisional mechanisms are dominating the radiative processes was used to check whether the plasma satisfies the LTE condition or not. We have used the Ca (I) emission line at 422.67 nm to check the LTE criterion [12, 14, 27]:

$$N_e (cm^{-3}) \geq 1.6 \times 10^{12} (\Delta E_{(eV)})^3 [T_{(k)}]^{1/2} \quad (11)$$

The density of the electron plasma for the cement sample is estimated to be ~10^{15} cm⁻³, determined through the electron temperature (T_e of about 9000 K) and energy difference (ΔE ~ 2.93 eV). Similarly, electron number densities computed for several cement varieties using the same Ca (I) line are around 10^{15} cm⁻³. This observation indicates that the N_e (1.1 ± 0.6) × 10^{17} cm⁻³ derived from broadened emission lines due to the Stark effect for all samples significantly exceeds the electron number-density calculated using McWhirter's criterion. Consequently, it suggests that the plasma can be observed as being in LTE.

3.2. Energy Dispersive X-ray (EDX)

The target samples that were examined by LIBS were studied using the energy-dispersive X-ray (EDX) system. Before EDX spectroscopical analysis, a layer of carbon was applied to the samples. This precaution was taken because carbon possesses a low atomic number, ensuring that its X-ray graph peak does not disrupt the peaks of other elements. To coat the samples, a carbon film containing vaporized carbon fiber was deposited. Carbon vaporized from the fiber due to the passage of electric current through it and deposited onto the sample. Optimal thicknesses for sample preparation for EDX analysis range from 5 nm to 20 nm.

EDX is an analytical technique that is frequently exploited in the elemental investigation of materials in the form of solid thin films, solid powder, liquid samples, or even a pellet, etc. [2, 34]. The production of X-rays in EDX connected with scanning-electron-microscopy (SEM) involves a two-step process. Initially, a high-energy electron beam impacts the sample surface, transferring some of its energy to the nuclear electrons of the target substance. This energy excites the electrons, causing them to be ejected from their shells, leaving behind vacancies (holes). Subsequently, electrons from shells at elevated energy levels fill these vacancies in shells with lower energy levels, emitting the energy difference (ΔE) in the form of X-rays. By employing this methodology, the energies of the emitted X-rays, which are distinctive to each element, and the corresponding signal intensities are utilized to quantify the elements present in the analyzed sample. The X-rays produced from the target are then captured using a 30 mm² Si (Li) detector. The compositional analysis of cement, Al-based alloys, and rare earth geological samples was carried out using an Oxford (X-MAX[N-20]) EDX instrument, coupled with an SEM instrument functioning at a 20 keV level [34, 35].

Fig. 5. The K_α K_β, L_α, and L_γ emission peaks detected from the cement target sample using EDX.
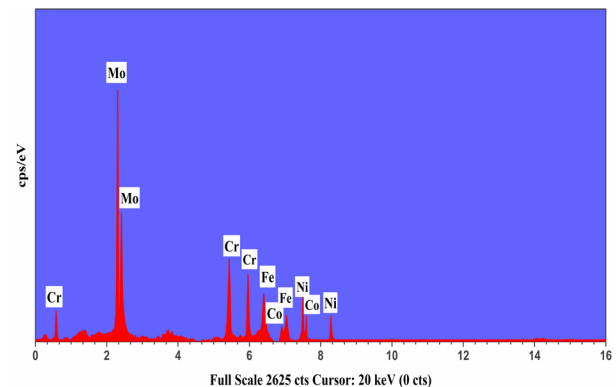
Fig. 6. Emission peaks: K_α and K_β in alloy sample with major molybdenum.

In this study, the results obtained using EDX for Mo-based alloys, cement, and rare earth geological samples are presented. The EDX spectra were collected from various spots on a homogeneous sample surface with an over-scan area of about ~100 μm^2 at an accelerating voltage of the electron beam of 20 kV. The EDX spectra illustrate the distribution of the energy spectrum of X-rays emanating from the specified point (micro-area) within the sample. Figure 5 reveals the detection of evident characteristic X-ray peaks, including K_α, K_β, L_α, and L_γ belong to various elements such as Al, Ca, Fe, K, Mg, Na, Si, and Sr in the cement sample. Similarly, the X-ray emission peaks of various elements are detected in the EDX spectra of the Mo-based alloy samples as presented in Figure 6.

3.3. Laser Ablation Time–of–Flight Mass Spectrometer (LA-TOF-MS)

Laser Ablation Time of Flight Mass Spectrometer (LA–TOF-MS) was also applied to observe the chemical weight of the rare earth geological, cement, and molybdenum-based alloy samples. There is no need for special pretreatment of the samples in the mass spectrometric analysis. We used the same pallets of the samples which were already used in the CF-LIBS analysis. The experimental configuration for LA–TOF-MS involves a stainless steel vacuum chamber with a 30 cm diameter, assisting ionization and extraction regions. This chamber is connected to a two-meter-long field-free flight tube, as shown in Figure 7. The extraction region is composed of three electrodes (3 cm × 3 cm), with two of them featuring 1 cm openings in the center covered by a fine tungsten mesh. To maintain a vacuum of

~1×10^{-6} mbar during the experiment, the chamber is linked to a turbo-molecular pump. Ion detection is carried out at the terminus of the flight tube using a channeltron electron multiplier detector (CEM-D), which is connected to an oscilloscope (Tektronix) having 500 MHz digital storage capacity [35-38].

In Figure 8, we show the mass spectrum of the Uraninite sample obtained using LA-TOF-MS to determine its relative chemical wt.%. The spectrum represents the signal corresponding to the ionic element along the y-axis and the arrival time of the ions at the detector is presented along the x-axis. An enlarged section is presented as an inset showing the peaks of the ingredient components present in the Uraninite sample. The peaks corresponding to the ions of the elements for instance Si$^+$, Ti$^+$, Mn$^+$, Na$^+$, Al$^+$, Ca$^+$, Fe$^+$, Ni$^+$, O+, and Zn$^+$ along with the ionic oxides such as LiO$^+$, SiO$^+$, FeO$^+$, MnO$^+$ and ZnO$^+$ are identified. A calibration curve is also presented as an inset to complement the elemental identifications. Interestingly, the signal corresponding to uranium ion is detected nearly at 88 microseconds [39].

Figure 9 illustrates a comparative analysis of individual elemental peaks from a rare earth ore sample, utilizing both the mass spectrum from the LA-TOF-MS system and the emission spectrum from the EDX system. Figure 9(a) displays the mass spectrum obtained from the LA-TOF-MS system, while Figure 9(b) illustrates the distinctive X-ray emission peaks representing different elements detected in the EDX spectrum of the geological mineral sample containing rare earth metals. In both spectra, the y-axis represents the relative intensity of the corresponding signals. The x-axis
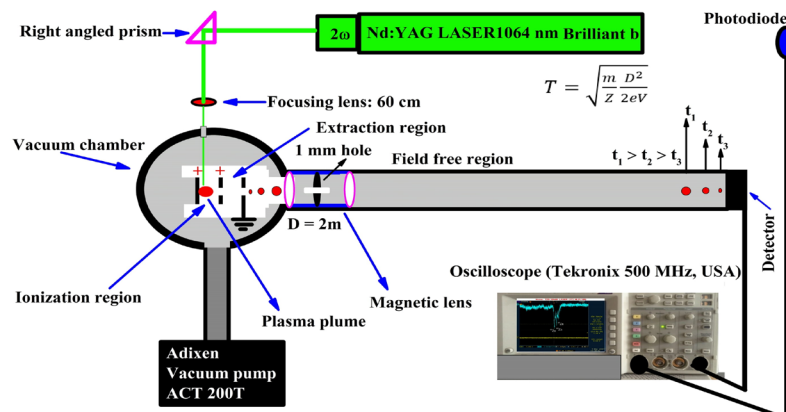
Fig. 7. A visual representation illustrating the configuration of the experimental arrangement for the LA-TOF-MS system, focusing on laser ablation/ionization processes.
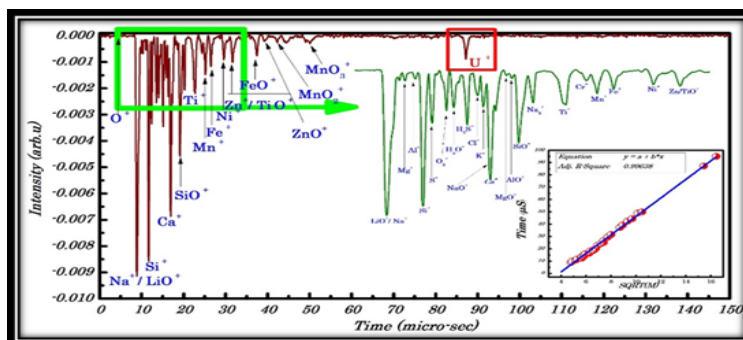
**Fig. 8.** A LA-TOF-MS spectrum of the Uraninite sample, inset shows the calibration curve.

of the LA-TOF-MS spectrum corresponds to time in microseconds (μs), while the x-axis of the EDX spectrum represents energy in kilo-electron volt (keV). Remarkably, the spectra obtained through EDX and LA-TOF-MS exhibit consistent element identification, except for oxygen. It is noteworthy, that these two methodologies are entirely distinct: the EDX data depict electron-induced emissions (of K_α, K_β, L_α, and L_γ, etc.) lines (X-ray region) from constituent elements along the x-axis, while the LA-TOF-MS mass spectrum illustrates the arrival times of ionic masses at the detector, where lighter ions arrive earlier than heavier ones. To enable comparison, we have aligned the x-axis to correlate the LA-TOF-MS ionic mass peaks with the corresponding EDX energy peaks of silicon and lanthanum. The comparison is highly favorable,

underscoring a close correlation in the compositional results acquired from both techniques. The element silicon emerges as the predominant component in both approaches, followed by C, Ca, Ti, Na, Mg, Fe, and rare earth metals such as lanthanum, cerium, and neodymium.

In Figure 10, we show the mass spectrum of the Mo-based alloy sample with the predominant peak corresponding to molybdenum, followed by peaks representing chromium (Cr), iron (Fe), cobalt (Co), and nickel (Ni). The y-axis of the graph illustrates the relative intensity of the ion signals, while the x-axis represents the arrival time of the ions. Inset (a) provides a well-resolved view of the peaks corresponding to Cr, Fe, Co, and Ni. This inset is particularly valuable as it showcases the individual peaks within the high-resolution time range of 10 to 12 microseconds, allowing for more precise identification and analysis of each element
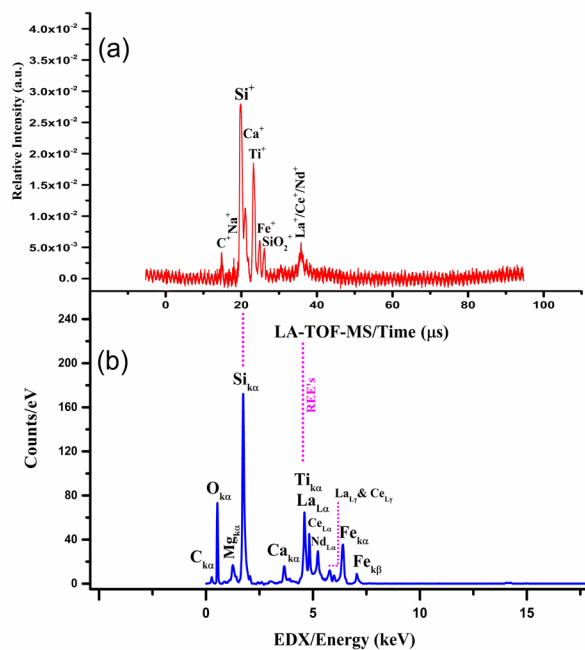
Fig. 9. (a) The quantitative comparison of LA-TOF-MS (laser energy fluence per pulse ~ 3 J/cm2) and (b) EDX (operated at 20 KeV) for analyzing the rare earth geological sample.
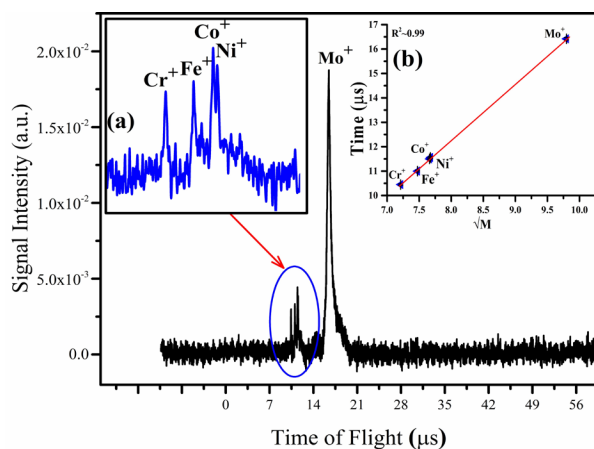
Fig. 10. The mass spectrum of the molybdenum-based alloy sample obtained using the LA-TOF-MS system. Inset (a) shows high-resolution peaks within a time scale from 10 to 12 μs, while (b) represents a linear regression calibration curve.
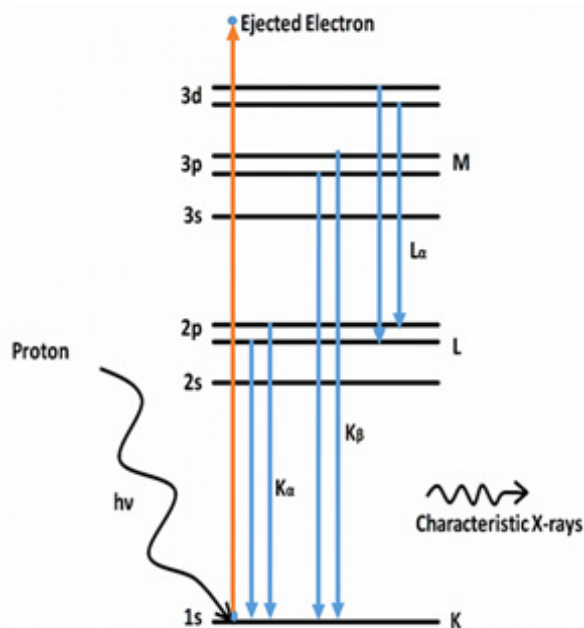
in the alloy. For a more detailed analysis, a linear regression calibration curve that correlates the square root of the mass with the time–of–flight of the ions is present as an inset (b). This calibration curve enhances the accuracy of mass determination in the analysis.

3.4. Proton–Induced X-ray Emission (PIXE)

In PIXE analysis, X-rays are generated by the excitation of the target atoms caused by a high-energy incident proton beam or alpha particles (^4_2He). The incident ions may experience further elastic or inelastic scattering during the interaction. The unstable excited target atoms decay to a stable energy state by restoring to their original electron configuration. The de-excitation of atoms may cause emission of the electromagnetic radiation in the form of X-rays (at a certain angle with the normal) which are characteristic of the excited atom as shown in Figure 11. The emission spectrum consists of various emission lines such as K, L, M, etc., generated by the electronic transitions. The elemental composition is estimated by registering the X-rays produced from the target sample [40, 41].

The PIXE analysis was conducted utilizing a high-power proton beam with an energy of around 3 MeV at a beam current of 5 nA. This proton beam was sourced from a 5 MV Pelletron-Tandem Accelerator (PTA) facility that is installed at the National Center for Physics in Islamabad, Pakistan. The facility serves as a crucial resource for providing the necessary particle acceleration for PIXE investigations in the experiments, allowing for precise and detailed elemental analysis [41, 42]. In Figure 12, the comparison between the two methodical techniques, for instance, LA-TOF-MS and PIXE for the cement target sample is presented. In Figure 12(a), the PIXE spectrum detects major peaks of elements such as Al, Ca, Si, Fe, Ti, and K. In Figure 12(b), we present the mass spectra from LA-TOF-MS, where a dominating ion peak of Ca is followed by K, Ti, Li, Na, Al, Si, Mg, Sr, and Fe, showing results consistent with the PIXE analysis of the same cement sample. The inset of the PIXE spectrum displays the same spectrum without fitting on a logarithmic scale. However, elements of light atomic numbers such as Li, Na, and Mg, and heavy atomic numbers such as Sr, remained undetected in the PIXE analysis due to the PIXE detection limit. The PIXE investigation of the cement target sample is carried out using the commercially available GUPIXWIN software. Interestingly, Ca in PIXE analysis is also a dominating constituent of the cement sample followed by Si and Fe.
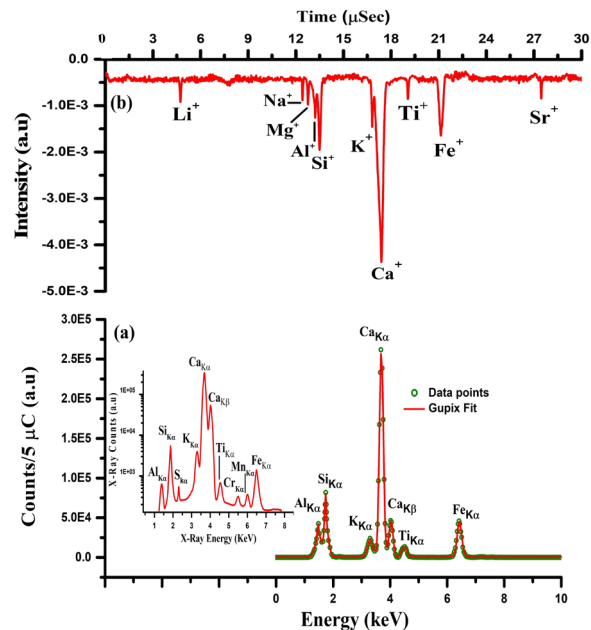
Fig. 12. A comprehensive spectral study of the cement sample through two analytical techniques: (a) PIXE spectrum with an inset showing spectrum without fitting and (b) LA-TOF-MS mass spectrum. The PIXE spectrum is supplemented by nonlinear fitting conducted with GUPIXWIN software. The PIXE data was obtained using a proton ion beam with an energy of around 3 MeV and a beam current of ~5 nA. These ions were sourced using a 5 MV PTA system.

Fig. 11. The schematic diagram of the PIXE experiment for the cement sample with a small thickness Δx.s.
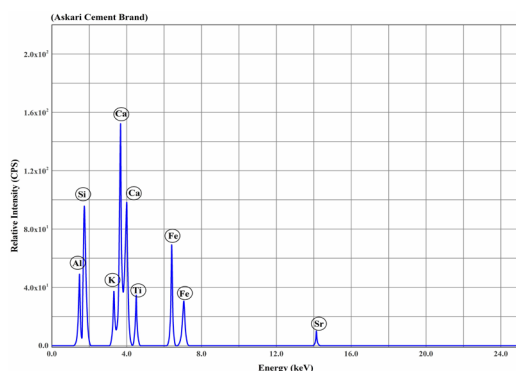
3.5. X-ray Fluorescence (XRF)

In the X-ray fluorescence (XRF) technique, an incoming X-ray knocks out an electron from one of the orbitals near the nucleus of an atom of the material. A positively charged hole (+) is generated in the orbital, which produces a stable state for another upper high-energy atomic electron. To reinstate the neutral or equilibrium state of an atom, an electron from a higher energy state falls into the lower state and the excess energy is emitted in the form of a fluorescent X-ray (K_α and K_β lines). The energy or wavelength, i.e., ($\lambda = 1240$ eVnm/E) corresponding to these emitted X-rays is specific for an element in the material to be analyzed. Hence, this emitted wavelength or energy of the X-ray photon makes XRF a fast analytical instrument for the analysis of elemental composition. Generally, the energy or wavelength of the emitted X-ray photon for a specific element is independent of the chemistry of the target sample [34, 35].

In various fields such as scientific, military, and forensic laboratories, metallurgical, and pharmaceutical industries, the XRF method is widely used for chemical weight analysis as the detection limits of this technique are much improved than SEM-EDX. However, this technique has limitations in the sample size but it yields excellent precision on samples having a flat surface of dimension greater than 1 mm². This analytical technique is also comparable with other techniques such as LIBS and LA-TOF-MS. These techniques can provide excellent elemental as well as mass isotopic analysis and can be employed as a primary reference to highlight the limitations and precision of other techniques. The elemental composition of the cement samples was investigated using the XRF technique. A JSX model-(3202M) setup, operating

at (5 to 50) kV with a current range of 0.01–1.0 mA and an energy resolution of 149 eV at 5.9 keV [34, 35], was employed for this purpose. The XRF energy spectrum shown in Figure 13 reveals major elements like Fe, Ca, and Si, while also indicating the presence of trace elements such as Sr, K, Ti, and Al in the cement sample. Although this technique can easily detect elements such as Na-U (Concentration > 100 ppm or 10-50 mg/kg), Na and Mg remain undetected, maybe due to the lower concentrations which are about 0.22% and 1.40%, respectively. Interestingly, the results are quite complementary in the domain of Al to Sr showing good compatibility between these two techniques.

To compare the analytical performance of the techniques, we performed a comprehensive analysis by comparing quantitative analysis for the cement sample. The quantitative results obtained from various techniques, including CF-LIBS, PIXE, EDX, XRF, and LA-TOF-MS are illustrated in Figure 14. Mainly, the quality control of Portland cement hinges on its major components, namely Al_2O_3, CaO, Fe_2O_3, and SiO_2. Following the standards set by the British authorities, the acceptable ranges for Ca, Si, Al, and Fe in Portland cement are (60% – 67%), (21% – 22%), (6%), and (3.5%), respectively [43-45]. Figure 14 illustrates that the cement sample falls within the specified limits for calcium, silicon, and iron. Remarkably, LIBS, EDX, XRF, and LA-TOF-MS methods consistently identify main elements such as Fe, K, Al, Ca, Ti, and Si. These results demonstrate an agreement in the composition obtained through the various analytical methods. However, PIXE analysis deviates notably for elements with atomic weights less than 20 (Li, Mg, Na) due to its lower detection limits. Additionally, the XRF technique's constrained detection capabilities result in the non-detection of Li and Na. This variance in PIXE and XRF results underlines the importance of considering the specific detection capabilities of each analytical technique in the comprehensive evaluation of cement composition.

4. RESULTS AND DISCUSSION

The application of EDX in combination with scanning electron microscopy (SEM) is commonly used for the qualitative and quantitative assessment of materials. The EDX depth profile usually reaches around 5 microns for the minimum

Fig. 13. XRF spectrum of cement under high vacuum with 50 kV anode voltage and 1 mA anode current.
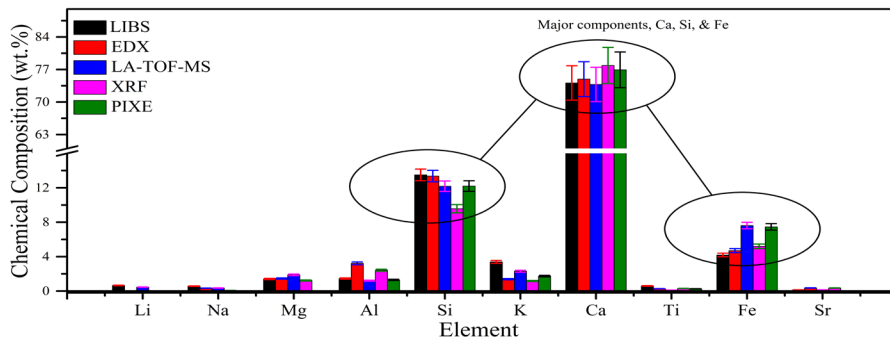
Fig. 14. A comparative analysis of the chemical weight % of the cement sample through various diagnostic techniques, including CF-LIBS, EDX, LA-TOF-MS, XRF, and PIXE.

detectable mass, with a detection limit of 0.01 wt.% according to theoretical calculations. For bulk materials, the limit is typically 0.1 wt.%, while for light elements, usually less than 10 atomic number, it's approximately 1-2 wt.%. Complex materials tend to have a detection limit greater than 5 wt.%. Therefore, under the optimized conditions for multielement analysis, the EDX analysis can only identify elements present in concentrations exceeding 0.1 wt.%. In this work, major elements with concentrations greater than 10 wt.%, such as Si and Ca, are consistently identified as predominant components with all analytical techniques. This highlights the reliability of EDX in identifying elements at relatively higher concentrations and reveals its role in both qualitative and quantitative material analysis, particularly for major components with significant presence.

In this study, the XRF technique was applied to examine the same set of samples. XRF analysis is suitable for multi-elemental analyses of several materials, containing soils, rocks, sediment, paint, herbal medicines, and cement, and in the construction industry for verifying the metallic composition. The XRF technique typically provides a depth profile reaching ~100 microns, with detection limits for most elements ranging from 2 to 20 ng/cm^2 for micro, and thin solid samples, aerosols, and liquids. The results of this study confirm that when the chemical wt.% of an ingredient in the sample exceeds 0.01 wt.% and the size range of the target sample is in millimeters in diameter or larger, more precise analysis and quantification of elements can be achieved. It's important to note that certain elements, specifically Mg and those with relatively lower concentrations compared to Mg, remained undetected in this analysis. This is due to the smaller concentrations of those elements in the sample,

as well as a limitation characteristic of the XRF technique. However, the technique successfully identified major elements with concentrations exceeding 10 wt.%, demonstrating its effectiveness in analyzing and quantifying elements present in significant amounts.

PIXE employs proton beams for analysis owing to their small energy loss in the target sample. The limit of detection in PIXE investigation is influenced by the X-ray spectrum from the environment, primarily generated by proton collisions of less than 1.5 to 2 MeV. An optimal proton energy for PIXE analysis falls in the range of 3 to 5 MeV. Remarkably, PIXE analysis exhibits low sensitivity to elements for instance C, H, Li, Mg, N, Na, and O due to their absorption in the X-ray detector's detection window. Conversely, its sensitivity is high when it comes to metallic elements and heavy elements in alloys or metallic samples. As a result, PIXE proves particularly suitable for studying biological, metallic alloy, or geological samples containing elements like Ca, Fe, Si, Sr, and Ti, etc. In the context of this study, elements such as Al, Ca, Fe, K, Si, and Ti were efficiently detected and quantified by PIXE, demonstrating its robust compatibility with LIBS and other diagnostic methods.

In LA-TOF-MS, there is no specific limit on the sample size or dimension. It needs a few mJ energy to ablate the sample surface. Once the sample is ablated and plasma is formed the only thing which needs to be done is the accelerating voltages across the metallic plates under a high vacuum. The mass spectra of LA-TOF-MS, (as shown in Figures 8 to 10), demonstrate that all the elements detected by LIBS are also present in these mass spectra. These results also reveal that both the

analytical techniques such as EDX and PIXE are in good agreement with the LA-TOF-MS. However, in the case of light elements, PIXE is unable to detect the lower Z elements but the LA-TOF-MS technique shows a good detection sensitivity.

In this work, a limited number of LIBS analyses were presented using geological, cement, and alloy samples. From these results, it is evident, that it is possible to differentiate between the samples of various natures by comparing the LIBS spectra and there is a good reproducibility of the LIBS analysis. Both qualitative and quantitative investigations of a sample can be conducted without producing scratches to the material's surface. The LIBS technique provides a depth profile extending to approximately hundreds of microns with a limit of detection varying from 10–50 ppm. In the current study, LIBS results consistently demonstrated a reliable detection limit, specifically showcasing the ability to detect elements such as Li to Sr within the cement analysis and C to Nd within the analysis of rare earth mineralogical samples. This highlights the use of LIBS in achieving both qualitative and quantitative insights into distinct sample compositions. Furthermore, the results obtained through LIBS exhibited reliability with those achieved using the LA-TOF-MS technique. Additionally, the analysis of major elements in the samples, such as Si, Ca, Ti, Fe, and Sr, conducted through EDX, PIXE, and XRF techniques also aligns well with the findings from LIBS and LA-TOF-MS. However, it is important to highlight an inconsistency observed when analyzing light elements, specifically Li, Na, and Mg, using EDX, PIXE, and XRF. In these examples, the results from the three techniques diverge, indicating a variation in their ability to accurately detect and quantify such lighter elements.

5. CONCLUSIONS

Different analytical techniques, including LIBS, LA-TOF-MS, EDX, PIXE, and XRF, have been employed to perform both qualitative and quantitative analyses on different varieties of samples. The LIBS qualitative analysis involved capturing emission spectra from a micro-plasma generated at 532 nm, with a pulse energy of 110 mJ, laser irradiance around ~2.8 GW/cm^2, and an integration time of 1 ms. The findings from LIBS demonstrate its rapid growth as a technique for chemically quantifying elements in diverse materials. Furthermore, the combination of LIBS with an LA-TOF-MS proved to be an effective and complementary approach for both isotopic and elemental analysis. Comparative analyses of geological, cement, and metallic alloy samples using LIBS were performed in sequence with results obtained from LA-TOF-MS, EDX, PIXE, and XRF. LIBS emerged as a rapid and micro-destructive technique, offering a relatively cost-effective solution. The incorporation of LIBS with LA-TOF-MS has been identified as the optimal analytical method for the quantitative elemental analysis of geological ores containing rare earths, cement, nephrite, and metallic alloy samples.

6. ACKNOWLEDGMENTS

7. CONFLICT OF INTEREST

The authors declare no conflict of interest.

8. REFERENCES

1. R. Noll, C. Fricke-Begemann, S. Connemann, C. Meinhardt, and V. Sturm. LIBS analyses for industrial applications–an overview of developments from 2014 to 2018. *Journal of Analytical Atomic Spectrometry* 33(6): 945-956 (2018).

2. A. Fayyaz, U. Liaqat, K. Yaqoob, R. Ahmed, Z.A. Umar, and M.A. Baig. Combination of laser-induced breakdown spectroscopy, and time–of–flight mass spectrometry for the quantification of CoCrFeNiMo high entropy alloys. *Spectrochimica Acta Part B: Atomic Spectroscopy* 198: 106562 (2022).

3. G.S. Senesi. Laser-Induced Breakdown Spectroscopy (LIBS) applied to terrestrial and extraterrestrial analogue geomaterials with emphasis to minerals and rocks. *Earth-Science Reviews* 139: 231-267 (2014).

4. V. Palleschi. Laser-induced breakdown spectroscopy: Principles of the technique and future trends. *ChemTexts* 6: 1-16 (2020).

5. S.S. Harilal, B. O'Shay, M. Tillack, and M.V. Mathew. Spectroscopic characterization of laser-induced tin plasma. *Journal of Applied Physics* 98(1): 013306-7 (2005).

6. E. Tognoni, G. Cristoforetti, S. Legnaioli, V. Palleschi, A. Salvetti, M. Müller, U. Panne, and I. Gornushkin. A numerical study of expected accuracy and precision in calibration-free laser-induced breakdown spectroscopy in the assumption of ideal analytical plasma. *Spectrochimica Acta Part B: Atomic Spectroscopy* 62(12): 1287-1302 (2007).

7. D.A. Cremers, and L.J. Radziemski (Eds.). Handbook of laser-induced breakdown spectroscopy. *John Wiley & Sons* (2013).

8. Z. Wang, M.S. Afgan, W. Gu, Y. Song, Y. Wang, Z. Hou, W. Song, and Z. Li. Recent advances in laser-induced breakdown spectroscopy quantification: From fundamental understanding to data processing. *TrAC Trends in Analytical Chemistry* 143: 116385 (2021).

9. G. Guo, G. Niu, Q. Shi, Q. Lin, D. Tian, and Y. Duan. Multi-element quantitative analysis of soils by laser induced breakdown spectroscopy (LIBS) coupled with univariate and multivariate regression methods. *Analytical Methods* 11(23): 3006-3013 (2019).

10. S. Zhang, X. Wang, M. He, Y. Jiang, B. Zhang, W. Hang, and B. Huang. Laser-induced plasma temperature. *Spectrochimica Acta Part B: Atomic Spectroscopy* 97: 13-33 (2014).

11. A. Ciucci, M. Corsi, V. Palleschi, S. Rastelli, A. Salvetti, and E. Tognoni. New procedure for quantitative elemental analysis by laser-induced plasma spectroscopy. *Applied spectroscopy* 53(8): 960-964 (1999).

12. Q. Abbass, N. Ahmed, R. Ahmed, and M.A. Baig. A comparative study of calibration free methods for the elemental analysis by laser induced breakdown spectroscopy. *Plasma Chemistry and Plasma Processing* 36: 1287-1299 (2016).

13. K.S. Singh, and A.K. Sharma. Spatially resolved behavior of laser-produced copper plasma along expansion direction in the presence of static uniform magnetic field. *Physics of Plasmas* 23(12): 122104 (2016).

14. S.S. Harilal, B.E. Brumfield, N.L. LaHaye, K.C. Hartig, and M.C. Phillips. Optical spectroscopy of laser-produced plasmas for standoff isotopic analysis. *Applied Physics Reviews* 5(2): 021301 (2018).

15. Z. Wang, C. Yan, J. Dong, T. Zhang, J. Wei, and H. Li. Acidity analysis of iron ore based on calibration-free laser-induced breakdown spectroscopy (CF-LIBS) combined with a binary search algorithm (BSA). *RSC Advances* 6(80): 76813-76823 (2016).

16. J. Peng, W. Xie, J. Jiang, Z. Zhao, F. Zhou, and F. Liu. Fast quantification of honey adulteration with laser-induced breakdown spectroscopy and chemometric methods. *Foods* 9(3): 341 (2020).

17. A. Safi, B. Campanella, E. Grifoni, S. Legnaioli, G. Lorenzetti, S. Pagnotta, F. Poggialini, L. Ripoll-Seguer, M. Hidalgo, and V. Palleschi. Multivariate calibration in Laser-Induced Breakdown Spectroscopy quantitative analysis: The dangers of a 'black box'approach and how to avoid them. *Spectrochimica Acta Part B: Atomic Spectroscopy* 144: 46-54 (2018).

18. D. Diaz, A. Molina, and D.W. Hahn. Laser-induced breakdown spectroscopy and principal component analysis for the classification of spectra from gold-bearing ores. *Applied Spectroscopy* 74(1): 42-54 (2020).

19. P. Inakollu, T. Philip, A.K. Rai, F.Y. Yueh, and J.P. Singh. A comparative study of laser induced breakdown spectroscopy analysis for element concentrations in aluminum alloy using artificial neural networks and calibration methods. *Spectrochimica Acta Part B: Atomic Spectroscopy* 64(1): 99-104 (2009).

20. J.B. Sirven, B. Bousquet, L. Canioni, L. Sarger, S. Tellier, M. Potin-Gautier, and I.L. Hecho. Qualitative and quantitative investigation of chromium-polluted soils by laser-induced breakdown spectroscopy combined with neural networks analysis. *Analytical and Bioanalytical Chemistry* 385: 256-262 (2006).

21. Z.A. Umar, U. Liaqat, R. Ahmed, and M.A. Baig. Detection of lead in soil implying sample heating and laser-induced breakdown spectroscopy. *Applied Optics* 60(2): 452-458 (2021).

22. T. Takahashi, B. Thornton, T. Sato, T. Ohki, K. Ohki, and T. Sakka. Partial least squares regression calculation for quantitative analysis of metals submerged in water measured using laser-induced breakdown spectroscopy. *Applied Optics* 57(20): 5872-5883 (2018).

23. T. Zhang, S. Wu, J. Dong, J. Wei, K. Wang, H. Tang, X. Yang, and H. Li. Quantitative and classification analysis of slag samples by laser induced breakdown spectroscopy (LIBS) coupled with support vector machine (SVM) and partial least square (PLS) methods. *Journal of Analytical Atomic Spectrometry* 30(2): 368-374 (2015).

24. E. Mal, R. Junjuri, M.K. Gundawar, and A. Khare. Optimization of temporal window for application of calibration free-laser induced breakdown spectroscopy (CF-LIBS) on copper alloys in air employing a single line. *Journal of Analytical Atomic Spectrometry* 34(2): 319-330 (2019).

25. F.O. Borges, J.U. Ospina, G.H. Cavalcanti, E.E. Farias, A.A. Rocha, P.I. Ferreira, G.C. Gomes, and A. Mello. CF-LIBS analysis of frozen aqueous solution samples by using a standard internal reference and correcting the self-absorption effect. *Journal of Analytical Atomic Spectrometry* 33(4): 629-641 (2018).

26. J.A. Aguilera, and C. Aragón. Multi-element Saha–Boltzmann and Boltzmann plots in laser-induced plasmas. *Spectrochimica Acta Part B: Atomic Spectroscopy* 62(4): 378-385 (2007).

27. A. Mansoori, B. Roshanzadeh, M. Khalaji, and S.H. Tavassoli. Quantitative analysis of cement powder by laser induced breakdown spectroscopy. *Optics and Lasers in Engineering* 49(3): 318-323 (2011).

28. J.A. Aguilera, and C. Aragón. Characterization of a laser-induced plasma by spatially resolved spectroscopy of neutral atom and ion emissions.: Comparison of local and spatially integrated measurements. *Spectrochimica Acta Part B: Atomic Spectroscopy* 59(12): 1861-1876 (2004).

29. O. Samek, D.C. Beddows, J. Kaiser, S.V. Kukhlevsky, M. Liska, H.H. Telle, and A.J. Whitehouse. Application of laser-induced breakdown spectroscopy to in situ analysis of liquid samples. *Optical Engineering* 39(8): 2248-2262 (2000).

30. A. De Giacomo, M. Dell'Aglio, O. De Pascale, S. Longo, and M. Capitelli. Laser induced breakdown spectroscopy on meteorites. *Spectrochimica Part B: Atomic Spectroscopy* 62(12): 1606-1611 (2007).

31. D.D. Pace, R.E. Miguel, H.O. Di Rocco, F.A. García, L. Pardini, S. Legnaioli, G. Lorenzetti, and V. Palleschi. Quantitative analysis of metals in waste foundry sands by calibration free-laser induced breakdown spectroscopy. *Spectrochimica acta part B: Atomic Spectroscopy* 131: 58-65 (2017).

32. J.M. Gomba, C. D'Angelo, D. Bertuccelli, and G. Bertuccelli. Spectroscopic characterization of laser induced breakdown in aluminium–lithium alloy samples for quantitative determination of traces. *Spectrochimica Acta Part B: Atomic Spectroscopy* 56(6): 695-705 (2001).

33. Atomic spectra database, NIST (2024). https://dx.doi.org/10.18434/T4W30F.

34. A. Fayyaz, U. Liaqat, Z.A. Umar, R. Ahmed, and M.A. Baig. Elemental analysis of cement by calibration-free laser induced breakdown spectroscopy (CF-LIBS) and Comparison with laser ablation–time-of-flight–mass spectrometry (LA-TOF-MS), energy dispersive x-ray spectrometry

(EDX), x-ray fluorescence spectroscopy (XRF), and proton induced x-ray emission spectrometry (PIXE). *Analytical Letters* 52(12): 1951-1965 (2019).

35. N. Ahmed, R. Ahmed, Z.A. Umar, and M.A. Baig. Laser ionization time of flight mass spectrometer for isotope mass detection and elemental analysis of materials. *Laser Physics* 27(8): 086001 (2017).

36. Z.A. Umar, U. Liaqat, R. Ahmed, and M.A. Baig. Classification of nephrite using calibration-free laser induced breakdown spectroscopy (CF–LIBS) with comparison to laser ablation–time-of-flight–mass spectrometry (LA–TOF–MS). *Analytical Letters* 53(2): 203-216 (2020).

37. A. Jabbar, M. Akhtar, S. Mehmood, N. Ahmed, Z.A. Umar, R. Ahmed, and M.A. Baig. On the detection of heavy elements in the Euphorbia indica plant using laser-induced breakdown spectroscopy and laser ablation time of flight mass spectrometry. *Journal of Analytical Atomic Spectrometry* 34(5): 954-962 (2019).

38. N. Ahmed, U. Liaqat, M. Rafique, M.A. Baig, and W. Tawfik. Detection of toxicity in some oral antidiabetic drugs using LIBS and LA-TOF-MS. *Microchemical Journal* 155: 104679 (2020).

39. J.O. Thompson, S.T. Alavi, J.R. Walensky, and A.G. Suits. Time of flight mass spectrometry with direct extraction of a uranium plasma. *International Journal of Mass Spectrometry* 445: 116190 (2019).

40. K. Ishii. PIXE and its applications to elemental analysis. *Quantum Beam Science* 3(2): 12 (2019).

41. W. Akram, K. Shahzad, A. Awais, I. Ahmad, M. Arif, I. Ahmad, and M. Madhuku. Roadside dust contamination with toxic metals along industrial area in Islamabad, Pakistan. *Nuclear Science and Techniques* 25(3): 1-6 (2014).

42. A. Awais, J. Hussain, M. Usman, W. Akram, K. Shahzad, T. Ali, I. Ahmad, and M. Maaza. The charge state distribution of B, C, Si, Ni, Cu and Au ions on 5 MV Pelletron accelerator. *Nuclear Science and Techniques* 28: 1-5 (2017).

43. G.N. Pandey, and S.D. Shukla (Eds.). A Textbook of Chemical Technology. *Vikas Publishing House, New Delhi* (1978).

44. N. Furman (Ed.). Standard Method of Chemical Analysis (6th ed). *Van Nostrand Reinhold Co. New York* (1962).

45. G.H. Jeffery, J. Bassett, J. Mendham, and R.C. Denney, (Eds.). Vogel's Textbook of Quantitative Chemical Analysis, 5th Edition. *Longman Scientific and Technical, Harlow, UK* (1989).